

Characterizing the Automatic Tube Potential Selection Feature for a CT Simulator
with the Mercury 4.0TM Phantom

By

Li Yuan

M.Sc., Brown University, 2023

Thesis

Submitted in partial fulfillment of the requirements for the
Degree of Master of Science in Medical School at Brown University

PROVIDENCE, RHODE ISLAND

MAY 2023

This thesis by Li Yuan is accepted in its present form
by the Medical School as satisfying the
thesis requirements for the degree of Master of Science

Date _____

Dr. Michael Oumano

Approved by the Graduate Council

Date _____

Dr. Thomas A. Lewis

ACKNOWLEDGMENTS

I would like to acknowledge many individuals for helping me during my master's study at Brown University. Particularly, I would like to express my sincere gratitude to my advisor Dr. Michael Oumano to provide the opportunity, knowledge and support that enabled this study. I would also like to thank him for his continuous support, patience, and guidance throughout the past two years.

I would also like to thank the program director Dr. Eric E. Klein, my committee members Dr. Edward Walsh, Prof. Michelle Schwer and Dr. Jian Liu for generously offering their time, suggestions and goodwill throughout the preparation and review of this document.

Thanks to Lauren Perugini, administrative coordinator of the Medical Physics Graduate Program, for her never-ending encouragement and helpfulness.

Neusoft Medical Systems (a manufacture of computed tomography scanners) provided the Mercury phantom used in this study. I would like to thank Neusoft for such generous support.

A special thanks to my family – my wife Jieying, and my daughter Helena – for their love and support. I would also like to thank my parents and parents-in-law for their love and prayers.

Table of Contents

Chapter 1. Introduction	3
Chapter 2. Methods	5
A. Materials and Equipment.	5
A. 1. Mercury 4.0™ phantom:	5
A. 2. Siemens CT Simulator	5
B. Examination Protocols	7
B. 1. Automated tube current modulation assessment.....	8
B.2. General Radial Noise distribution analysis.	8
C. Experiments	9
C. 1. Experiment 1: Tube potential and Radiation dose (single section)	9
C. 2. Experiment 2: Tube potential and Radiation dose (two successive sections).....	9
C. 3. Experiment 3: HU Variation	9
D. Radiation Dose and Image Quality Analysis	9
Chapter 3. Results	11
Automated tube current modulation assessment.....	11
General Radial Noise Distribution Analysis.....	13
Experiment 1. Tube potential and radiation dose (single section).....	14
Experiment 2. Tube Potential and Radiation dose (two successive sections).....	20
Experiment 3. HU Variation.	21

Chapter 4. Discussion.....	23
Chapter 5. Conclusion	28
MATLAB Source Code	29
Reference	36

Table of Tables

Table 1. The major acquisition parameter of the base and ATPS protocols.	7
Table 2. The scan parameters and the radiation dose	11
Table 3. Raw data that reported after each examination.	14
Table 4. The difference and percentage of CTDI _{vol} reduction ranges of each section.....	14
Table 5. The average gray value of the background and each insert	15
Table 6. The CNR values of five different material inserts.	16
Table 7. The lesion detectability index of each material under base and ATPS protocols.	20
Table 8. The difference and percentage of CTDI _{vol} reduction ranges of two successive sections.....	20
Table 9. The HU values of different material inserts that scanned with different tube potentials.	22

List of Illustration

Figure 1. Mercury 4.0™ phantom.....	5
Figure 2. The CT Simulator (Simens Healthcare SOMATOM Confidence)	6
Figure 3. Part of the base protocol configuration.....	7
Figure 4. The way to pick ROIs for radial noise distribution analysis.....	8
Figure 5. Automated tube current modulation feature	12
Figure 6. General radial noise distribution (noise level vs. distance to center).....	13
Figure 7. The noise level varied radially in the phantom due to beam filtration.	17
Figure 8. The NPS of five different-diameter sections scanned with the ATPS and base protocols	19
Figure 9. Screenshots of 160 mm section that scanned with different tube voltage.....	21
Figure 10. Screenshots of 360 mm section that scanned with different tube voltage	21
Figure 11. The smallest section and the largest section	26

**Abstract of Characterizing the Automatic Tube Potential Selection Feature for a CT Simulator
with the Mercury 4.0™ Phantom, By Li Yuan, Degree ScM.**

Brown University, May 2023

Objectives: To elaborate on the significance of enabling the automatic tube potential selection (ATPS) feature on Computed Tomography (CT) simulators. Furthermore, evaluate the effect of this change on optimal tube potential, radiation dose, and diagnostic quality with phantoms of various sizes. Propose the best approach to apply ATPS to routine CT scans from a radiation oncology perspective.

Methods: Assessed the machine's automated tube current modulation (ATCM) and analyzed the ATCM's effect on image quality with the Mercury 4.0™ phantom. The five different diameter cylindrical sections of the phantom were scanned with a standard manually-selected 120 kilovoltage peak (kVp) protocol and an ATPS-enabled protocol, respectively. Radiation doses, contrast-to-noise ratios (CNRs), noise distributions, noise power spectra (NPS), and lesion detectabilities were compared between the standard and ATPS protocols. All phantom sections were also scanned with all available fixed tube potentials and the resultant changes in Hounsfield Unit (HU) values were compared.

Results: The effective mAs has been modulated for different dimension of the sections by enabling the ATCM feature of the CT simulator. The tube potentials selected by the ATPS algorithm for the small and standard size sections (diameter < 360 mm) were less than 120 kV, while the largest section (diameter = 360 mm) resulted in a higher tube potential (140 kV). The radiation dose (CTDI_{vol}) for all scans with ATPS were lower than the standard protocol by 2% to 33%. The variations of the HU values of the same materials acquired with different tube voltages are up to ± 50 (for bone).

Conclusions: In this thesis, we are the first to report AEC performance for any CT system at a kVp greater than 120. The lower potentials were automatically selected only for the phantom's small and standard size sections. The magnitude of the CNR, the NPS plots, and the detectability of various materials showed the image quality was maintained. However, the variation of the HU value of the same

materials scanned with different potentials was significant. A change of HU values > 50 HU for bone was observed for all kVp stations other than 120 kVp. The ATPS should therefore be disabled on this particular CT simulator unless accounted for via multiple kVp-specific electron density curves or other special software are applied.

Chapter 1. Introduction

There are two types of CT units: diagnostic scanners and specialty scanners, in radiation oncology, called CT simulators¹. From the appearance, they have only slight differences: the bore's dimension and the couch surface's shape. Although both share most features and functionality, they have been developed with focus on different clinical purposes. The diagnostic scanner aims to provide the best IQ at the lowest possible dose for physicians to diagnose disease. In contrast, the CT simulator provides 3-D data on the spatial location of everything within the body for the purpose of radiotherapy treatment planning. The CT number from the CT simulator will be converted into electron density by the TPS before planning. For TPS systems, only one electron density curve can be used at a time for this conversion. So, the accuracy of CT numbers from CT simulators is essential. Our study was focused on a CT simulator, and we took the accuracy of CT numbers into account when we assessed the effect of ATPS. Our study's analysis and conclusion may not apply to diagnostic CT scanners.

Tube potential is one of the major acquisition parameters of CT simulators and dramatically affects both radiation dose and image quality (IQ). Although vendor-dependent, x-ray CT simulators typically run at 120 kVp for generic scanning while other options like 70, 80, 100, and 140 kVp are also available². Previous research reported that lower tube potentials could be applied to pediatric patients to avoid unnecessary radiation doses while maintaining IQ^{3 4 5}. In addition, lowering the tube potential increases IQ for contrast-enhanced imaging tasks, like CT angiography (CTA)⁴. On the other hand, the highest tube potential (140 kV) is necessary to reduce the scan time and limit motion artifacts for obese patients with a body mass index (BMI) of about $40 \text{ kg}/\text{m}^2$ or more^{6 7}.

Generally, better IQ can be achieved with a higher dose to the patient. However, radiation dose should be minimized as much as possible regarding a given clinical task. The balance between obtaining a high-quality image and keeping the radiation dose delivered to the patient as low as reasonably achievable (ALARA) should be achieved during the CT scanning⁸. As one of the solutions, automatic tube current

modulation (TCM or ATCM) system reduces the tube current as the attenuation path decreases, and the same IQ can be achieved while the radiation level is lowered ². Similar to ATCM, the automatic tube potential selection (ATPS) algorithm provides the lowest radiation dose by considering the x-ray attenuation of each patient's body and the diagnostic task of imaging ³. ATPS can reduce the patient's dose by between 18% to 40% without impairing CNR ^{3 9}. Even though ATPS has such advantages, it has not been as widely adopted by most clinical practices as ATCM.

The Mercury 4.0TM phantom consists of five different diameter cylindrical sections, which can be used to simulate the different sizes of patients. It was designed to evaluate the performance and effectiveness characterization of the automatic exposure control (AEC) system ¹⁰.

For further treatment, this study aimed to utilize the Mercury 4.0TM phantom to assess the performance of ATPS-enabled CT protocols and address the limitations and concerns of applying the ATPS feature to clinical practices.

Chapter 2. Methods

This is a pure phantom-based study, and there is no institutional review board approval required.

A. Materials and Equipment.

A. 1. Mercury 4.0™ phantom:

This type of phantom consists of five different diameter cylindrical sections, and each section has two subsections (Figure 1): one uniform and the other containing cylindrical inserts of 1451 CT HE solid water, air, bone (50% CaCO₃), polystyrene, and HE iodine (10mg/ml).

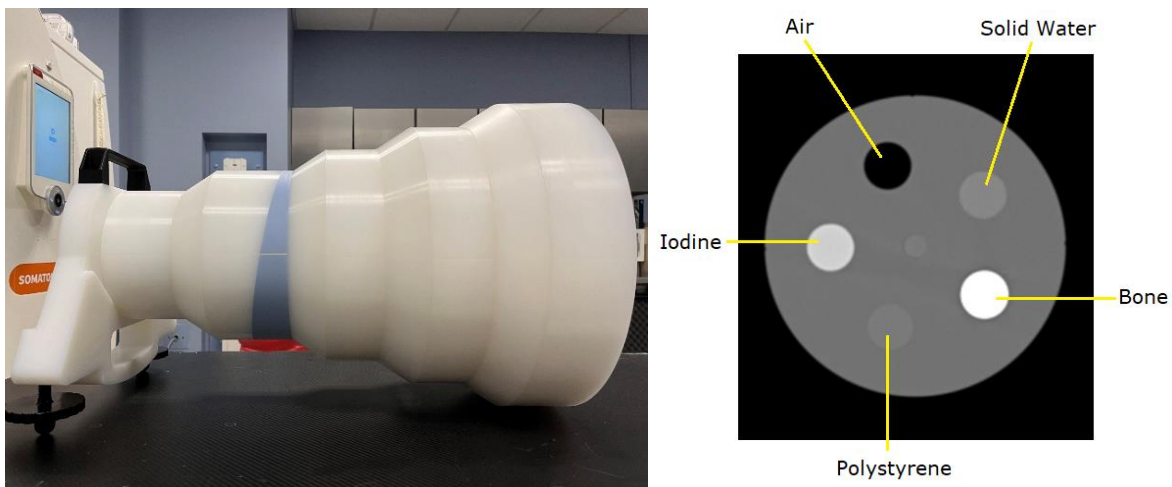


Figure 1. Mercury 4.0™ phantom, consisting of five sections of different diameters with tapered transitional sections (left). This phantom is designed to assess system noise, resolution, and lesion detectability of the CT system. Each section contains five inserts of different materials (right).

A. 2. Siemens CT Simulator (Siemens Healthcare, SOMATOM Confidence)

The CT simulator used in this study was equipped with AEC software integrated with ATCM and ATPS (Figure 2). *CARE Dose 4D* is the mA-modulation (ATCM) algorithm. It adjusts the tube current according to the topogram (z-axis modulation) and in real-time with angular (x-y axis modulation),

whereby the actual attenuation of a patient is measured during the scan ⁹. *CARE kV* is the ATPS algorithm that utilizes the information in topogram images to automatically select the tube potential. It is highly dependent on the diagnostic task and patient size ⁶.



Figure 2. The CT Simulator (Siemens Healthcare SOMATOM Confidence), featured by CARE Dose4D (automated tube current modulation) and CARE kV (automated tube potential selection).

Multiple studies ^{11 12 13 14} suggested that, after activating both ATCM and ATPS, the lower tube potentials (< 120 kV) were automatically selected as optimal tube potential to improve or maintain the IQ for a patient with BMI < 40 kg/m².

B. Examination Protocols

Base protocol: We chose a routine adult abdomen protocol as our base protocol. The major acquisition parameters are listed in Table 1.

Protocol	Slice (mm)	CARE kV Setting	kV	Rotation (s)	Pitch	Kernel	Ref. mAs	CARE Dose4D	CARE kV
Base	3	N/A	120	1	1.0	Br38*	250	On	Off
ATPS	3	3	120	1	1.0	Br38*	250	On	On

Table 1. The major acquisition parameter of the base and ATPS protocols. *Br38 indicates Body Regular 38 cm.

ATPS protocol: The CARE kV feature was then activated for the base protocol, and reference mAs set to 250.

The following steps must be completed very carefully before each scanning.

1. Align the phantom with the isocenter precisely.
2. Set the reference mAs (210) and reference tube potential (120 kV), which is based on a standard-sized adult patient weighing 75kg¹⁵.
3. Ensure CARE Dose4D (ATCM feature) was enabled (Figure 3).
4. For ATPS protocol scanning, enable the CARE kV by selecting ‘On’ from the drop-down menu.
5. At least one topogram must be acquired before acquiring the CT scan.

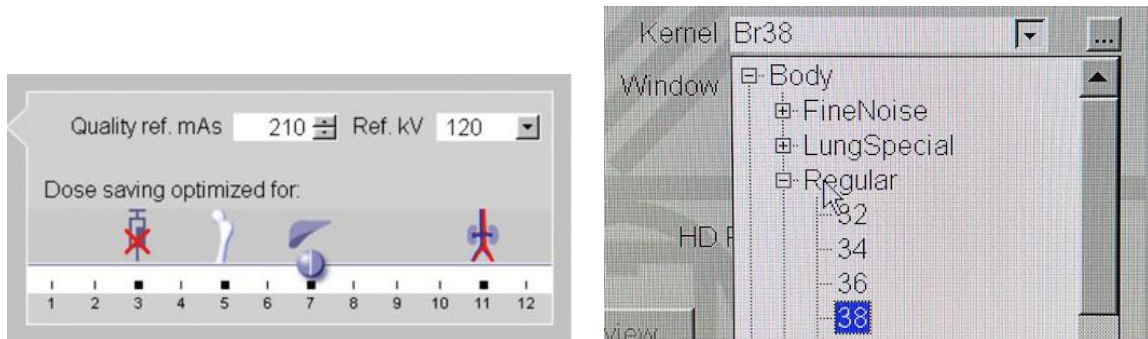


Figure 3. Part of the base protocol configuration. We enabled CARE Dose4D (ACTM) and disabled CARE kV (ATPS). We choose the Br38 (Body Regular) kernel for both protocols.

B. 1. Automated tube current modulation assessment.

Before implementing the designated experiments, we assessed the effect of the automated tube current modulation feature of the CT simulator. We scanned the whole phantom with three different fixed tube voltages: 100 kV, 120 kV, and 140 kV, and set the same pitch ratio for each group of experiments.

B.2. General Radial Noise distribution analysis.

We picked several groups of ROIs from each slice of the CT output (DICOM files), and each group has eight squares with the same radius from the center (Figure 4). The average noise values of eight squares were used to represent the noise level for that radius.

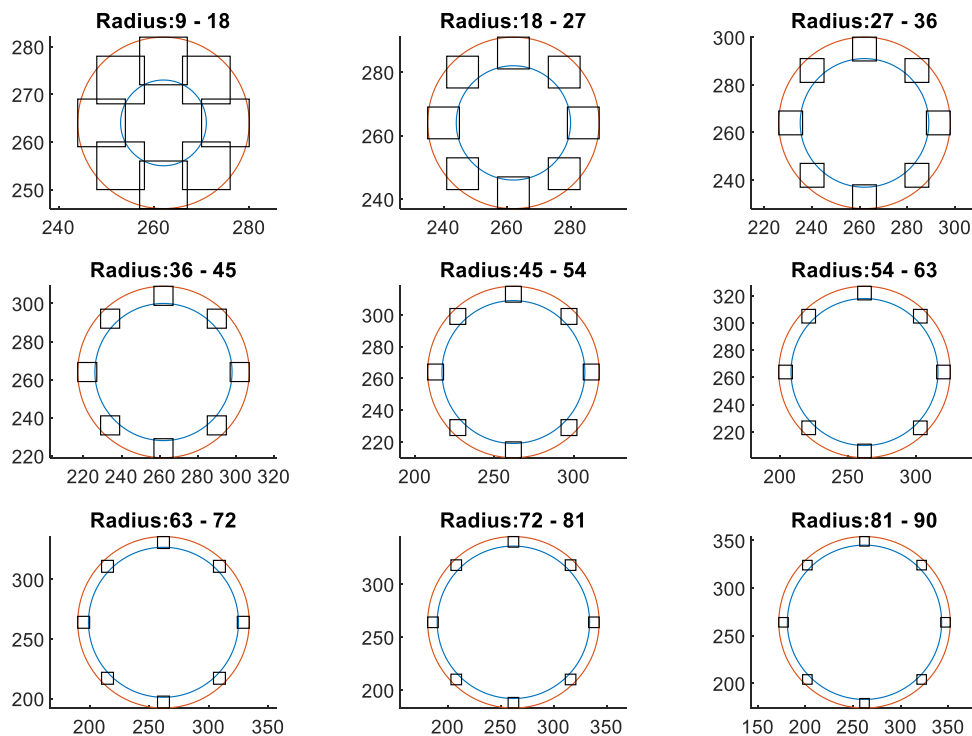


Figure 4. The way to pick ROIs for radial noise distribution analysis, each group sample to have the same radius value to the center of the section. The average noise value of eight squares was used to represent the noise level of that radius.

C. Experiments

C. 1. Experiment 1: Tube potential and Radiation dose (single section)

We scanned the phantom's five cylindrical sections with the base and ATPS protocols, respectively. For each pair of scans, the optimal tube potential selected by ATPS were recorded and compared with the fixed tube potential (120 kV) in the base protocol. The tube potential, effective tube current-time product, and CT Dose Index ($CTDI_{vol}$) were reported.

C. 2. Experiment 2: Tube potential and Radiation dose (two successive sections).

Instead of scanning five single sections, we scanned four successive two-diameter sections with the base and ATPS protocols.

C. 3. Experiment 3: HU Variation

We scanned the smallest and the largest diameter sections with all available tube potentials: 70, 80, 100, 120, and 140 kV, and measured the HU value of each material insert under different tube potentials.

D. Radiation Dose and Image Quality Analysis

For each scan with the ATPS protocol, the CT simulator prompted the optimal x-ray tube potentials, effective tube current-time values (eff. mAs equation. 1), and $CTDI_{vol}$. The average and standard deviation of the background HU values, and the average of five inserts HU values were measured using ImageJ¹⁶. Furthermore, all these HU values were used to calculate the CNR of each material by equation 2². Normalized radial noise distributions (normalized noise vs. distance to center) and noise power spectrum (NPS) (equation. 3) distributions were plotted for each section with and without APTS by an in-house MATLAB program. The HU values for experiment 3 were collected by ImageJ¹⁵. The lesion

detectability of each material within each section was calculated by equation. 4¹⁷ and reported by Imquest.

$$effective\ mAs = mA \times \frac{rotation\ time}{pitch}$$

Equation 1. Effective tube current-time values equal tube current multiplied rotation time and divided by pitch

$$CNR = \frac{(\bar{X}_s - \bar{X}_{bg})}{\sigma_{bg}}$$

Equation 2. CNR equal the difference of average gray scale between ROI and background divided by standard deviation of background. \bar{X}_s is the average gray scale of a ROI, \bar{X}_{bg} is the average gray scale of ROI in the background, σ_{bg} is the standard deviation of pixel gray scale of ROI.

$$NPS(f_x, f_y) = \left| \iint [I(x, y) - \bar{I}] e^{-2\pi i(xf_x + yf_y)} dx dy \right|^2$$

Equation 3. Equation of the noise power spectrum (NPS). f_x is the frequency corresponding to the x-dimension. f_y is the frequency corresponding to the y-direction. $I(x, y)$ is the gray scale of each pixel, and \bar{I} is the mean value of the image function $I(x, y)$.

$$d'^2 = \frac{[\iint W(r)^2 \cdot TTF(r)^2 \cdot V(r)^2 r dr]^2}{\iint W(r)^2 \cdot TTF(r)^2 \cdot V^4 \cdot NPS(r) r dr + \iint n_i \cdot W(r)^2 \cdot TTF(r)^2 \cdot NPS(r) r dr}$$

Equation 4. Equation of the lesion detectability of each material. $W(r)$ is the task function. $TTF(r)$ is the task transfer function, $V(r)$ is the visual response function, and $NPS(r)$ is the noise power spectrum function.

Chapter 3. Results

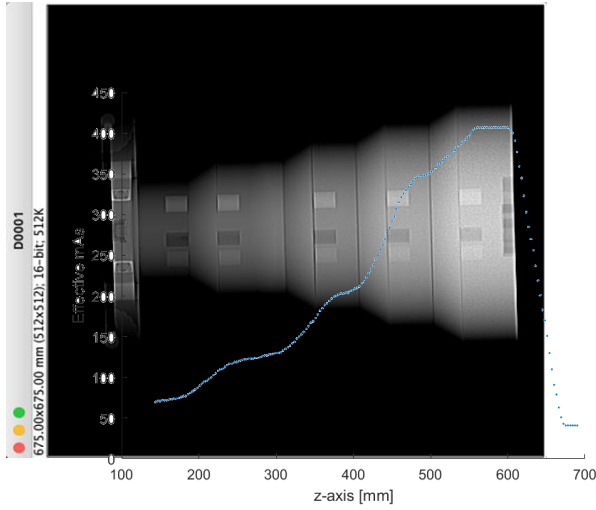
Automated tube current modulation assessment.

Automated Tube current modulation (ATCM) is one of the modern CT scanners and CT simulators' features that automatically adapt the x-ray tube current to the patient attenuation to achieve the desired level of image quality ¹⁸. The tube current is reduced as the attenuation path decreases, and the radiation dose level can be reduced consequently ². The modulation can be applied not only to the x-y plane but also to the z-axis of the patient. To assess the effect of ACTM characteristics along the z-axis, we scanned the whole phantom with different tube voltages (100 kV, 120 kV, and 140 kV) and two different pitch ratios (0.91 and 0.7). From Table 2, we found out that with the same pitch ratio, the higher tube voltage resulted in a higher radiation dose; with the same tube voltage, the higher pitch ratio resulted in a lower radiation dose. (The Table-2 data and Figure-5 images were acquired from Neusoft CT Simulator)

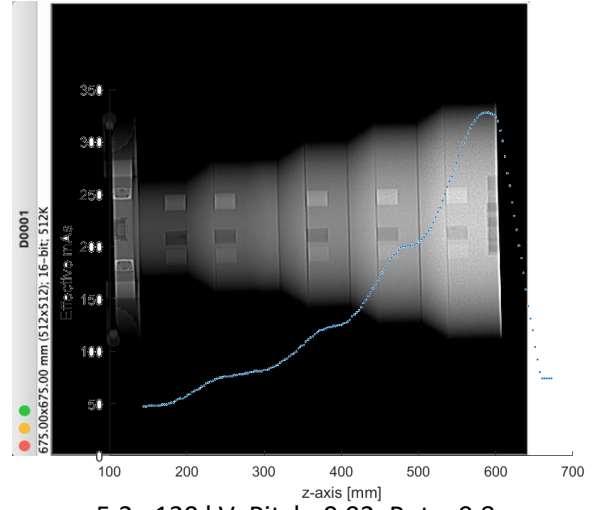
No.	kVp	Rotation Time (s)	Pitch	Ave. CTDI _{vol} (mGy)
1	100	0.8	0.92	7.26
2	120	0.8	0.91	8.64
3	140	0.8	0.91	9.04
4	100	1.0	0.7	11.73
5	120	1.0	0.7	13.34
6	140	1.0	0.7	38.69

Table 2. The scan parameters and the radiation dose were acquired for automated tube current modulation assessment. As we expected, the same pitch and higher tube voltage result in a higher dose. The same tube voltage and higher pitch ratio results lower radiation dose.

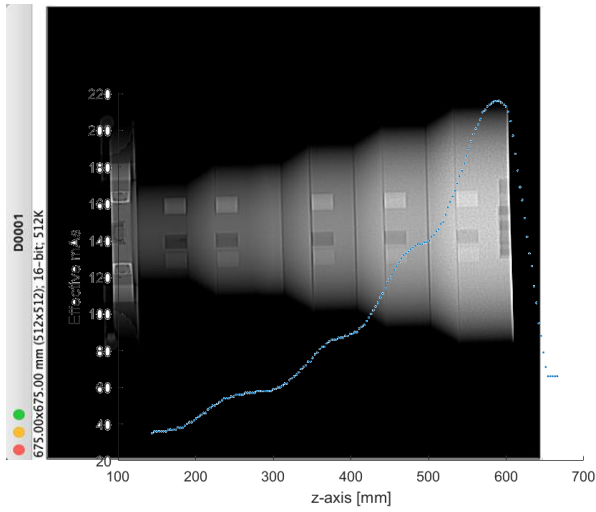
We extracted the tube current, rotation time, and pitch ratio from the DICOM files, calculated the effective mAs for each slice, put them together to plot the effective mAs vs. z-axis, and fused with the image of the phantom (Figure 5).



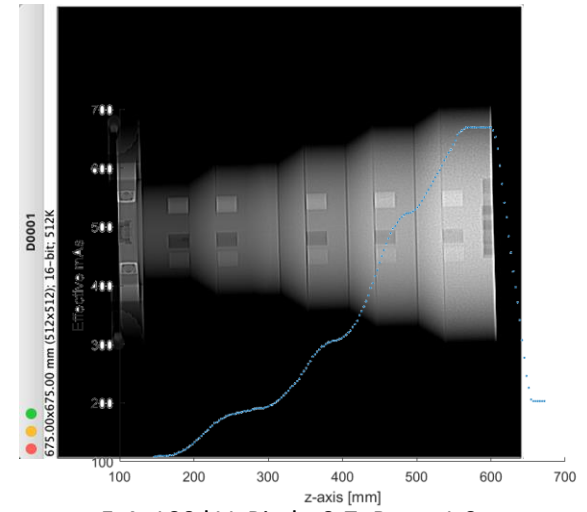
5.1. 100 kV, Pitch=0.92, Rot = 0.8s



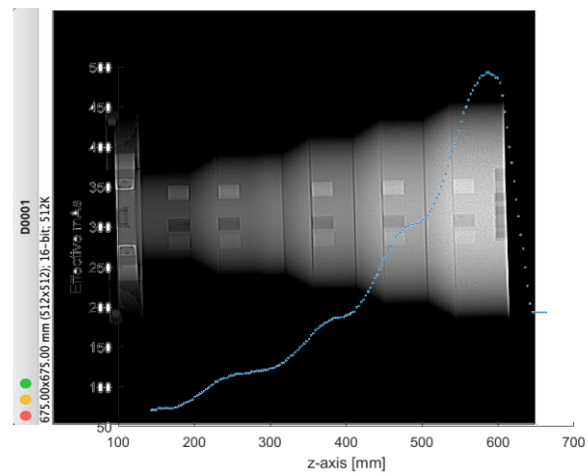
5.2. 120 kV, Pitch=0.92, Rot = 0.8s



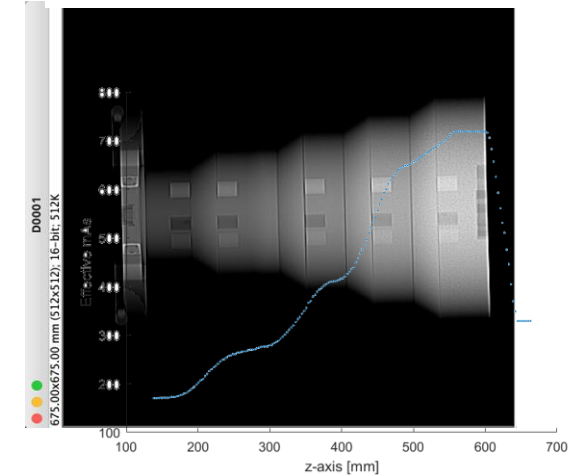
5.3. 140 kV, Pitch=0.92, Rot = 0.8s



5.4. 100 kV, Pitch=0.7, Rot = 1.0s



5.5. 120 kV, Pitch=0.7, Rot = 1.0s



5.6. 140 kV, Pitch=0.7, Rot = 1.0s

Figure 5. Automated tube current modulation feature has been assessed by plotting effective mAs vs. z-axis for different tube voltage (100 kV, 120 kV, and 140 kV) and different pitch ratio (0.92 and 0.7), respectively.

General Radial Noise Distribution Analysis

The noise level is highly dependent on the depth of ROI. The deeper the ROI, the higher noise will result. The Mercury 4.0™ phantom consists of five different dimensions of cylindrical sections, which are perfect to be used to reveal and visualize such noise distribution. Within the same section of the phantom, we plotted the noise of the same position within different sections. To make it more meaningful, we wrote a MATLAB script (Source Code 2) to put all five curves together to visualize the general radial noise distribution (Figure 6). As expected, the noise level is highly dependent on the ROI's depth and the section's dimension.

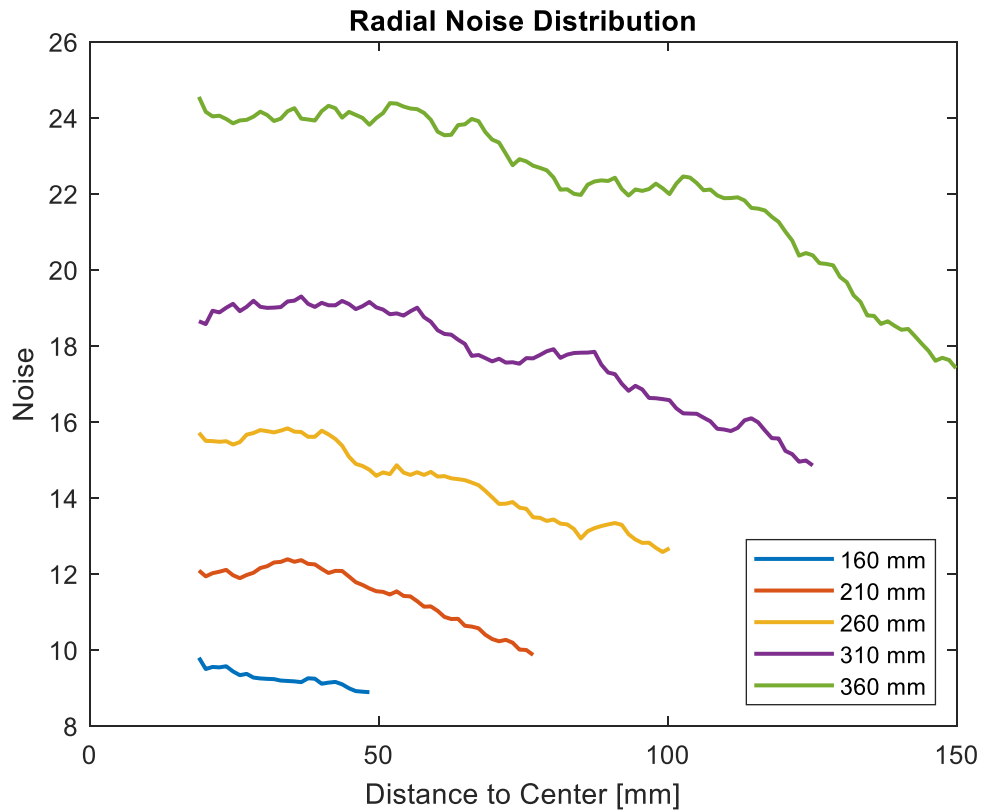


Figure 6. General radial noise distribution (noise level vs. distance to center) for five different dimensions of sections. As we expected, the noise level is higher when the ROI is close to the center, and the more depth of the ROI, the higher the noise level.

Experiment 1. Tube potential and radiation dose (single section).

The tube potentials automatically selected by ATPS were highly dependent on the diameter of the sections (from 70 kV to 140 kV). The smaller the diameter, the lower the tube potential and vice versa. The mAs values were also modulated by ATCM to maintain IQ for each examination. It did not share the same or opposite trend with tube potential. As expected, for the same diameter section, the $CTDI_{vol}$ acquired with the ATPS protocol was always lower than the value acquired with the base protocol (Table 3). The reductions ranged from 1.2% to 33.4% (Table 4).

Group	Diameter (mm)	CARE kV	kV	mAs	$CTDI_{vol}$ (mGy)
1-1	160	Off	120	83	6.7
		On	70	296	4.45
1-2	210	Off	120	105	8.48
		On	70	492	7.4
1-3	260	Off	120	146	11.8
		On	100	231	10.9
1-4	310	Off	120	208	16.8
		On	100	352	16.6
1-5	360	Off	120	345	27.9
		On	140	232	27.1

Table 3. Raw data that reported after each examination. Dose kV = Off: scanned with the base protocol; Dose kV = On: scanned with the ATPS protocol.

Group	Diameter (mm)	$\Delta CTDI_{vol}$ (mGy)	%CTDI
1-1	160	-2.25	-33.4%
1-2	210	-1.08	-12.7%
1-3	260	-0.9	-7.6%
1-4	310	-0.2	-1.2%
1-5	360	-0.8	-2.9%

Table 4. The difference and percentage of $CTDI_{vol}$ reduction ranges of each section.

CNR. We measured the average gray value of the background, and each insert within each section was scanned by the base and ATPS protocols (table 5). Then the CNR of five different inserts were calculated by equation 2 (Table 6). The ATPS protocol resulted in better CNR values for 60% of the CNR pairs of the five materials. The ATPS also resulted in better CNR values for 80% of the CNR pairs of high-density materials such as bone and iodine. The standard 120 kVp protocol resulted in better CNR values for 70% of the CNR pairs of low-density materials such as air and polystyrene, which is fat-mimicking.

Diameter (mm)	kV	\bar{X}_{bg}	σ_{bg}	\bar{X}_{air}	\bar{X}_{water}	\bar{X}_{bone}	$\bar{X}_{Polystyrene}$	\bar{X}_{iodine}
160	120	-94	3.686	-1002	-1.118	934	-38	277
	70	-144	4.656	-1002	1.506	1437	-87	524
210	120	-93	5.419	-1002	-2.326	908	-36	264
	70	-142	7.409	-1003	1.791	1411	-85	515
260	120	-80	9.034	997	-3.484	874	-35	248
	100	-93	8.844	-999	-2.005	991	-46	311
310	120	-78	10.304	-991	-4.385	844	-33	234
	100	-90	10.143	-991	-3.844	961	-43	296
360	120	-87	12.534	-983	-6.466	819	-33	223
	140	-79	13.191	-992	-4.188	762	-24	188

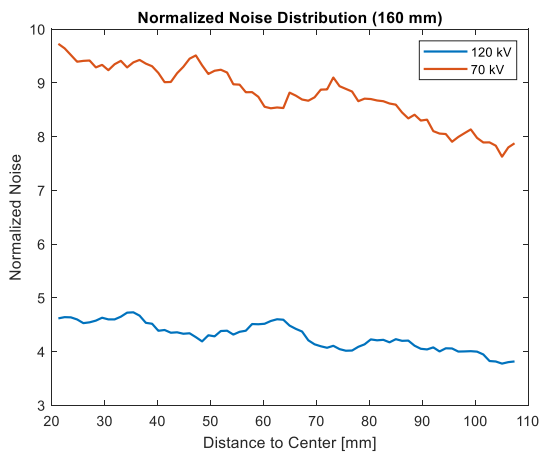
Table 5. The average gray value of the background and each insert that scanned with base and ATPS protocols.

Diameter (mm)	kV	CNR_{air}	CNR_{water}	CNR_{bone}	$CNR_{Polystyrene}$	CNR_{iodine}
160	120	-246.3	25.2	278.9	15.3	100.7
	70	-184.3	31.3	339.6	12.2	143.5
210	120	-167.7	16.7	184.7	10.5	65.9
	70	-116.2	19.4	209.6	7.7	88.7
260	120	119.2	8.5	105.6	5.0	36.3

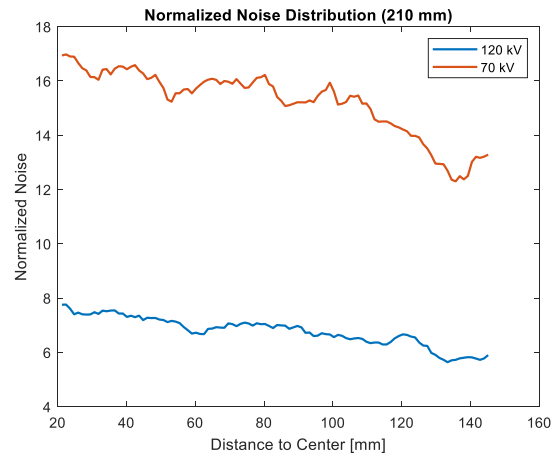
	100	-102.4	10.3	122.6	5.3	45.7
310	120	-88.6	7.1	89.5	4.4	30.3
	100	-88.8	8.5	103.6	4.6	38.1
360	120	-71.5	6.4	72.3	4.3	24.7
	140	-69.2	5.7	63.8	4.2	20.2

Table 6. The CNR values of five different material inserts.

Radial noise distribution. The noise varied radially in the phantom in all cases due to beam filtration (Figure 7). The noise level decreased as the location got farther away from the center of the phantom. As expected, higher tube voltage results in lower noise due to increasing penetrability of the x-rays. It turned out that the beam filtration we used works better (more radially-uniform noise) for small-diameter sections than for large-diameter sections in our study. The difference between minimum and maximum values of the curves in Figure 7 indicate the standard 120 kVp protocol generally results in more uniform images and less radial noise variability. The plots in Figure 7 were generated by MATLAB source code 3.



7.1



7.2

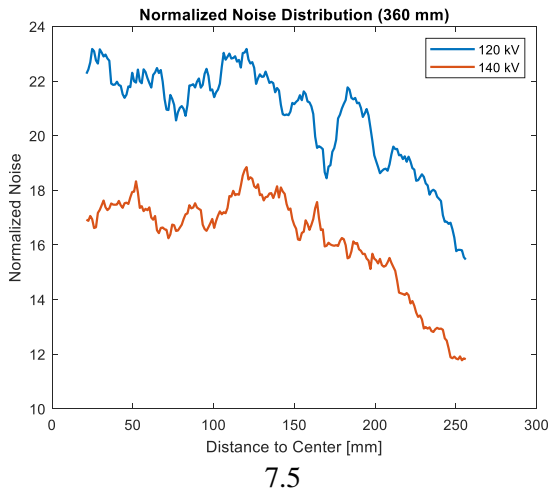
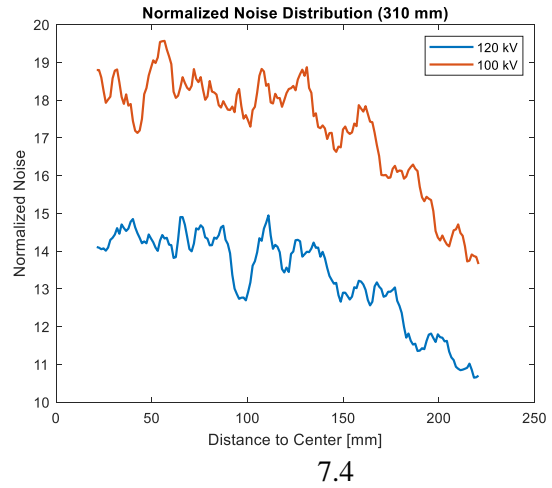
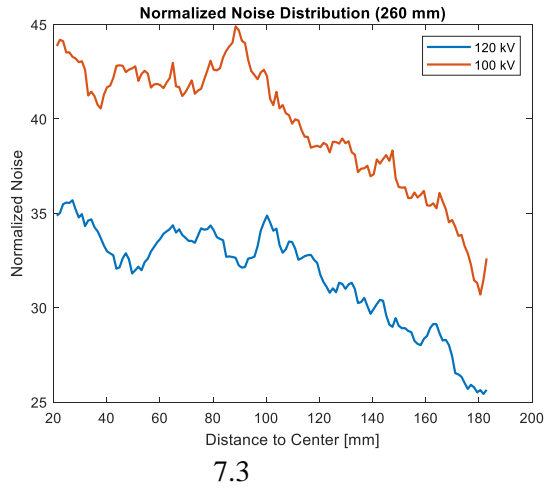
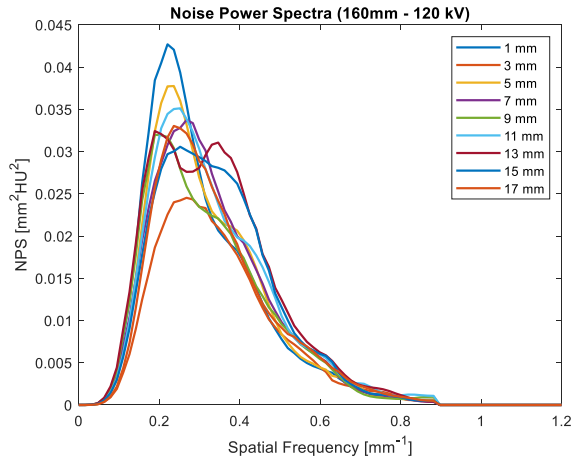
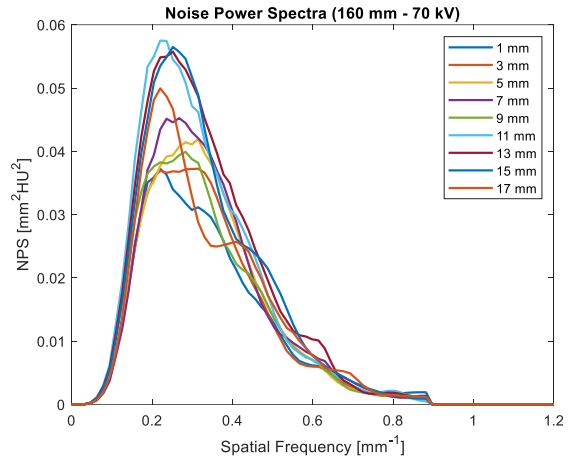


Figure 7. The noise level varied radially in the phantom due to beam filtration. As the sample location got far away from the center of phantom, the noise level decreased. The higher tube potential results in lower noise level.

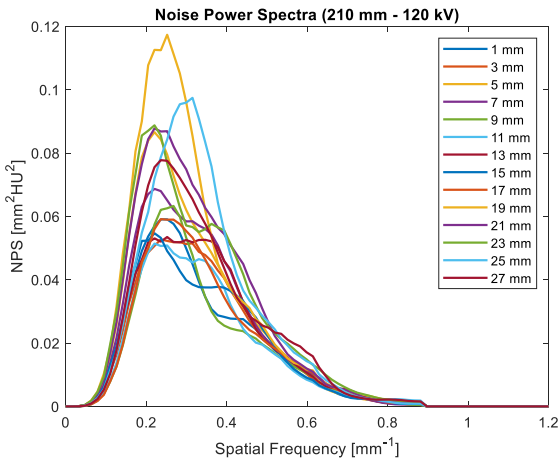
NPS distribution. The Noise-Power-Spectrum is a frequency-dependent breakdown of the variance. It describes how the noise propagates through an imaging system; thus, it can be used to examine the noise texture of an image. NPS can be calculated by equation 3. The NPS of sections scanned with the base and ATPS protocols were plotted side-by-side for the same diameter section (Figure 8). Because the noise/standard deviation of pixel values is equal to the integral of the one-dimensional (collapsed) NPS, the amplitude of the NPS increases for cases where raw noise increases. The similar NPS distributions of each pair of plots indicated essentially identical noise textures. All the following plots were generated by MATLAB source code 4.



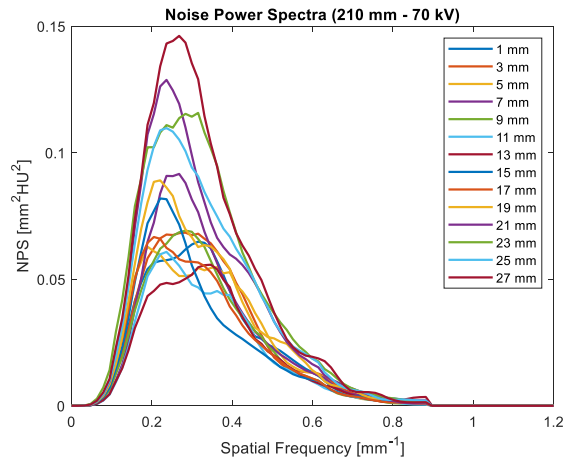
8.1.1



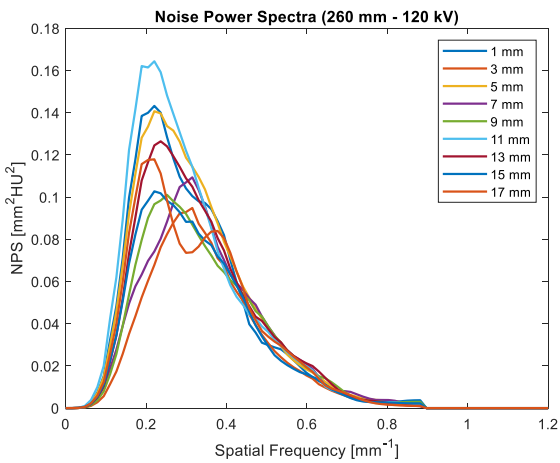
8.1.2



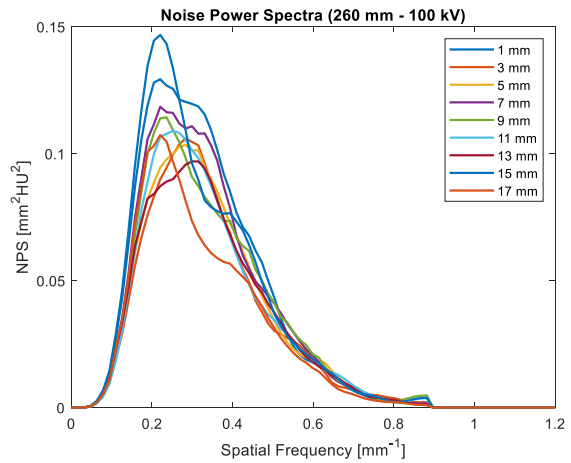
8.2.1



8.2.2



8.3.1



8.3.2

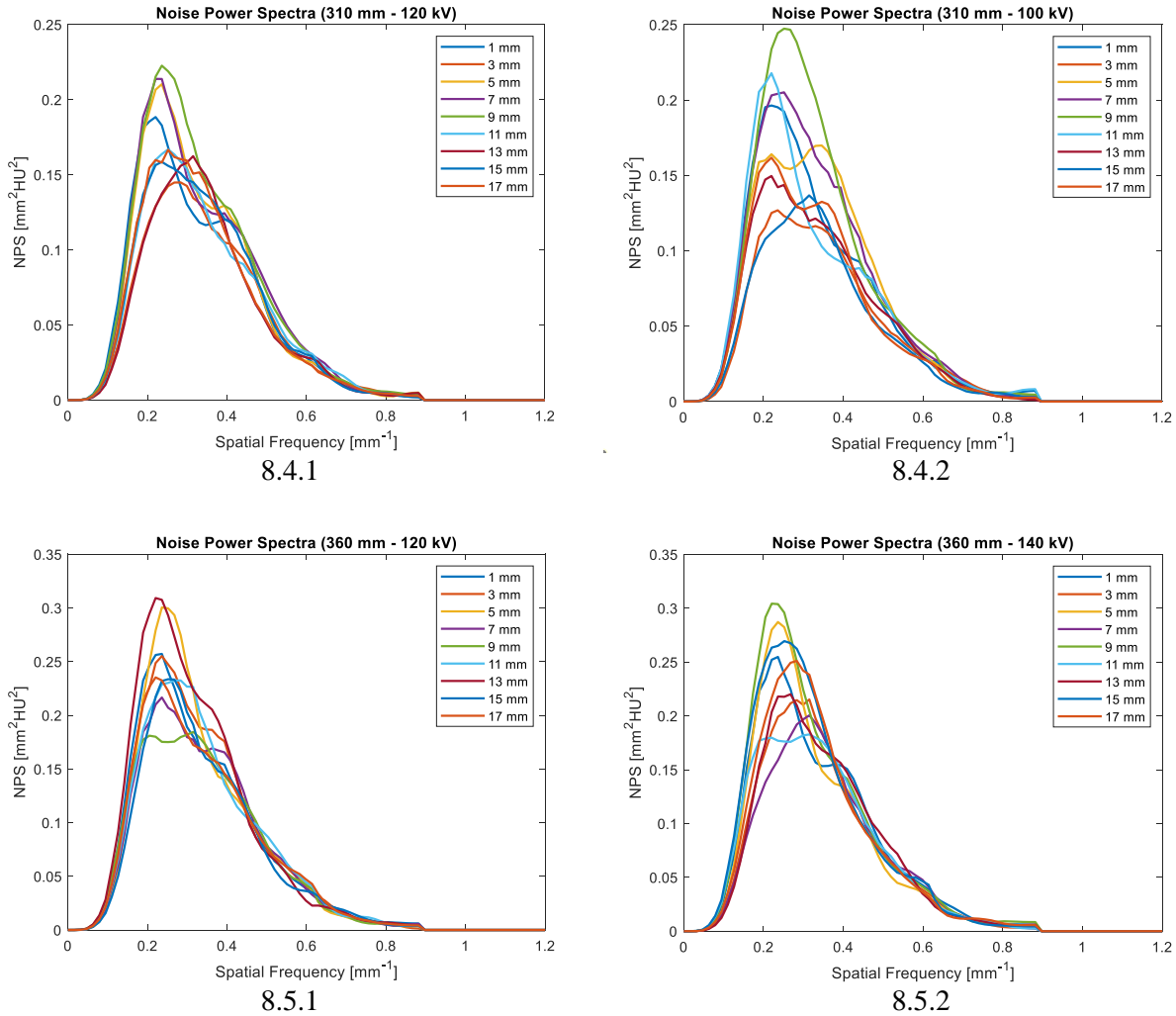


Figure 8. The NPS of five different-diameter sections scanned with the ATPS and base protocols were plotted side-by-side. The range of NPS and the shapes of each pair of plots are very closed, which indicate the same level of image qualities.

Lesion detectability index. For all the single sections, the lesion detectability indexes of each material acquired with the base and ATPS protocols were very close (Table. 7). The ATPS protocol resulted in better lesion detectability index for 68% of the time. The ATPS also resulted in higher lesion detectability index for 80% of the time for high-density materials. The ATPS and standard are even 50/50 for low-density materials.

Diameter (mm)	kV	d'_{air}	d'_{water}	d'_{bone}	$d'_{Polystyrene}$	d'_{iodine}
160	120	555.3	59.37	673.88	28.03	238.69
	70	382.81	67.66	740.93	25.75	307.86
210	120	455.53	47.93	539.58	26.7	191.59
	70	316.19	58.42	628.61	19.99	263.32
260	120	333.02	26.26	371.85	11.09	126.07
	100	347.19	32.13	445.66	15.21	164.96
310	120	309.09	23.62	332.51	13.77	110.91
	100	288.37	23.18	363.61	15.04	133.43
360	120	151.16	13.03	169.01	8.12	56.47
	140	166.85	13.96	161.23	8.13	51.56

Table 7. The lesion detectability index of each material under base and ATPS protocols.

Experiment 2. Tube Potential and Radiation dose (two successive sections).

In experiment 1, the ATPS resulted in 70, 70, 100, 100, 140 kVp for the 160, 210, 260, 310, and 360 mm sections of the phantom, respectively. In experiment 2, the ATPS resulted in 70, 100, 100, 140 kVp for the 160-210, 210-260, 260-310, 310-360 mm scans, respectively (table 8). It was confirmed that the ATPS automatically selected tube potentials based on the largest part of the phantom scanned.

Group	Diameter (mm)	$\Delta CTDI_{vol}$ (mGy)	%CTDI
2-1	160 – 210	-1.32	-17.4%
2-2	210 – 260	-0.99	-10%
2-3	260 – 310	-0.5	-3.5%
2-4	310 - 360	-0.4	-1.7%

Table 8. The difference and percentage of $CTDI_{vol}$ reduction ranges of two successive sections.

Experiment 3. HU Variation.

The contrast difference can be observed by naked eye from Figure 9 (160 mm section) and Figure 10 (360 mm section), which scanned with all available tube voltages (70 kV, 80 kV, 100 kV, 120 kV, and 140 kV). The difference is insignificant from the perspective of diagnostic purposes.

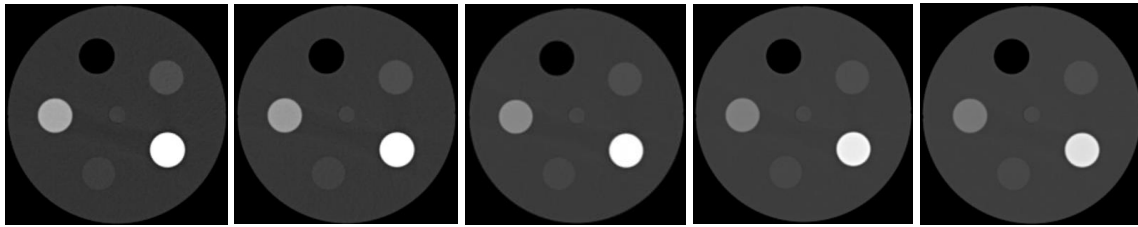


Figure 9. Screenshots of 160 mm section that scanned with different tube voltage (from left to right: 70 kV, 80 kV, 100 kV, 120 kV, and 140 kV). There is no significant difference from the naked-eye inspection.

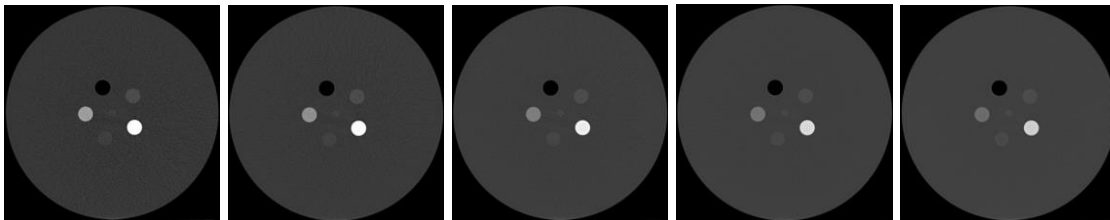


Figure 10. Screenshots of 360 mm section that scanned with different tube voltage (from left to right: 70 kV, 80 kV, 100 kV, 120 kV, and 140 kV). Similar to Figure 9, there is some contrast difference between these images, but not that significant.

HU values varied significantly with kVp (Table 9). Except for air, the variations of the other four materials are too significant to be used for treatment planning purposes in radiation oncology. Davis et al¹⁹ establish that CT numbers should not deviate by more than 20 HU for soft tissue or 50 HU for lung and bone.

Diameter (mm)	kV	Air	Solid Water	Bone	Polystyrene	Iodine
160	70	-1005	3.536	1447	-87	528
	80	-1007	1.453	1262	-70	447
	100	-1005	-0.428	1059	-48	341
	120	-1004	-0.652	938	-37	278
	140	-1005	-1.080	867	-29	238
360	70	-984	-2.417	1300	-80	472
	80	-985	-4.401	1129	-62	391
	100	-988	-3.918	941	-42	287
	120	-990	-6.200	830	-33	226
	140	-995	-5.325	768	-24	190

Table 9. The HU values of different material inserts that scanned with different tube potentials.

Chapter 4. Discussion

ATCM, as a specific implementation of AEC, automatically adapts the x-ray tube current to patient attenuation to a desired IQ²⁰. The overall effect of this feature is to use a different level of radiation for the parts of the body that have different attenuation. Most ATCM schemes result in lower dose and a more homogenous distribution of CT noise in the image along the z-axis².

Similar to ATCM, ATPS is one of the integrations of the AEC system, and it has become one of the standard features for modern CT simulators. The major advantages of ATPS have been discussed and demonstrated:

1. It complies with the ALARA principle by lowering the radiation dose without sacrificing the diagnostic image quality, especially for the pediatric patient^{3 4 5}.
2. It mitigates the technologist workload by reducing the number of protocols, thus minimizing the potential user's error^{2 18}.
3. It improves the image quality of certain diagnostic tasks by lowering tube potential, such as contrast-enhanced abdominopelvic CT and CTA^{4 21}.

Maintaining a given CNR is the main objective of the ATPS and allows for reduction of CTDI. For the large size of the patient, the first choice of optimal kV may exceed the power limitation of CT. In that case, the CT will choose the next-best and possible kV for a scan.

Scanning time and tube power limit are two factors that need to be taken into account during the tube voltage selection process. We suspect that when the tube power reaches its limitation and requires longer scan times, the ATPS algorithm will choose the next higher tube potential⁶. This either requires further testing to decipher manufactures' algorithm or clarification by the manufacturer. Assuming a reference kVp of 120, the ATPS will decrease the tube potential in most cases and increase the tube potential for an

obese patient. Radiation dose depends on the tube potential and the effective tube current (mAs). In that case, the lowest tube potential may not result in the lowest radiation dose ¹⁶.

Our study validated the dose reduction effect of ATPS-enabled CT protocols and assessed the image's quality by multiple metrics: CNR, NPS, Noise distribution, and lesion detectability index (d'). In addition, we addressed the therapeutic concern of applying ATPS to daily practices.

The Mercury 4.0TM phantom recently became available to evaluate CT AEC systems. Brinkley et al. recently evaluated the four smaller sections of the phantom to simulate neonate, young child, adolescent, and young adult abdominal diameters ⁴. Similarly, the pediatric anthropomorphic phantoms utilized in Papadakis et al.'s ³ report were all of smaller diameters. However, overweight and obese patients are prevalent in day-to-day clinical practices ²², so our study also took the largest section (diameter =360 mm) of the phantom into account. No study published to date has yet reported AEC performance for any CT system for a phantom this large. This is extremely important for characterizing performance at kVps greater than 120.

The results in Table 3 and Table 4 show that the tube potentials selected by ATPS were lower than 120 kV for the four small sections. The smaller the diameter of the section, the lower the potential was selected by ATPS, which is consistent with previous research ⁴. In contrast, the potential selected for the largest section was 140 kV in our experiment, which indicated that ATPS did not always reduce the tube potential. The ATPS algorithm stated by Papadakis et al ³ was the combination of tube potential and tube current determined by the specific patient size and diagnostic task. The diagnostic task can be interoperated with the CNR level of the CT examination. The data presented in Brinkley et al. report showed that keeping other configurations constant and reducing the CNR level of the scan required lower tube potential ⁴.

The radiation dose is not only determined by tube potential, but also the effective mAs¹⁰. The result in Table 4 shows that no matter which potential the ATPS selected, the effective mAs values were modulated accordingly and eventually reduced the CDTI_{vol} from 1.25% to 33.4%.

Gaining the same level of CNR within the limit capacity of the machine's generator power output is the primary goal of the ATPS algorithm. As expected, the result in table 6 shows that the CNR values of the same material under different protocols are generally very close or better for the ATPS. In the four small sections, the CNR acquired with the ATPS protocol were also higher than that acquired with the base protocol. That advantage did not apply to the largest section because contrast was reduced at the higher kVp.

Besides CNR metrics, we characterized the radial noise distribution, NPS distribution, and lesion detectability index to assess the image quality.

As Figure 6 shows, the noise is radially dependent and also varies with the section size. Clearly, the beam filtration we used was good for the small sections, but less so for the larger sections. This was surprising because the simulator should have automatically selected a bow-tie filter designed for body scans. These results indicate potential value in using the Mercury 4.0TM phantom for further bow-tie filtration analyses. The shapes of the NPS curves in Figure 8 of each pair's plots acquired from the base and ATPS protocol share the same pattern and range, which confirmed that the image qualities of the two scans were at the same level. In addition, the lesion detectability index in Table 7 was another indicator that the image quality acquired by the base and ATPS protocol was at the same level. Furthermore, the lesion detectability indexes of the same material within the same section acquired by the ATPS protocol were higher than those acquired by the base protocol for most circumstances in our experiment.

To make the phantom experiment closer to clinical practice, we designed the second group of experiments: changed the scan range from one single section to two successive sections to simulate the variation of the actual patient sizes during the scan. The trend of CDTI_{vol} shared the same result as we got

from the first group of experiments. In addition, the second group of experiments confirmed that the ATPS-selected tube potentials were determined by the thickest section of the phantom. This also explained why the full phantom scan did not always reduce the tube potential in previous research ⁴.

For the purpose of CT simulation in radiation oncology, the HU values acquired from the CT simulator would be imported into the treatment planning system (TPS). Thus, the accuracy of the HU value is essential. The biggest concern is that the non-fixed tube voltage of 120 kV would cause the electron density curve to shift and affect the accuracy of the following treatment. The third group of experiments was used to assess the shift of the electron density curve under different tube voltages (Figure 11). The plots of Figure 12 were generated by Source Code 5. The results in Table 9 indicated that except for the air, all the other materials' HU values have a variance as the tube voltage went away from the standard voltage of 120 kVp, and the HU variances were out of the acceptable tolerance range for a treatment plan (for soft tissue: ± 20 HU, for bone: ± 50 HU) ¹⁹. Another concern is that most CT simulators' HU values were calibrated with a fixed tube voltage of 120 kVp. Changing tube voltage settings would cause the CT performance to be unpredictable. Some of the vendors have already realized these concerns and developed a new reconstruction algorithm to compensate for such effects ²³, such as Siemens DirectDensity™.

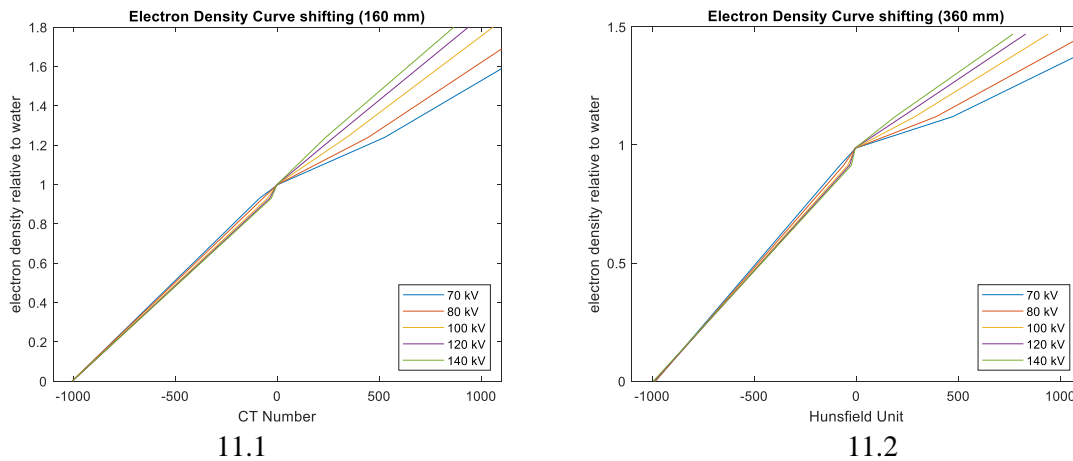


Figure 11. The smallest section (diameter = 160 mm) (4.a) and the largest section (diameter = 360 mm) (4.b) are used to assess the shift of the electron density curve under different tube voltages scanning. The HU variances were out of the acceptable tolerance range for a treatment plan (soft tissue: ± 20 HU, bone: ± 50 HU).

The first limitation of this study was that all the experiments were phantom-based and the background material of the Mercury 4.0™ phantom is polyethylene. However, using the equation in the AAPM TG 220 report ²⁴, we have determined that the water equivalent diameter (WED) of 360 mm section is 348 mm ¹⁰, which is a reasonable approximation of an obese patient. The thickness and organ attenuation of actual patients would also affect tube potential and current in a more complicated manner than in cylindrical phantom sections. Lastly, our research involved only a single Siemens CT simulator (SOMATOM Confidence). It is likely that there will be variability in performance across different makers and models.

Chapter 5. Conclusion

Our experiments validated that activating ATPS could reduce the overall radiation dose for both small and large patients while increasing or maintaining CNR levels. We are the first to report this in a phantom greater than 32 cm in diameter at a kVp greater than 120. The drawback of this operation is that ATPS-selected tube potentials other than 120 kVp resulted in HU values drifting outside the acceptable range for a treatment planning. HU values drifting will have minimal-to-zero clinical significance for many non-quantitative studies. However, from perspective of radiation oncology, this drifting will cause inaccuracy of electron density, thus the ATPS should therefore be deactivated on CT simulators unless perhaps advanced reconstruction software is used.

MATLAB Source Code

```
path = '13';
pre_name = strcat('mercury_phantom.CT.RTP_Thorax_[fac.',path, '.');

% Count the number of files in the directory
end_pos = size(dir(path),1)-2;

% Initiate two empty arrays
z = [];
eff = [];

for i= 1:1:end_pos
    file_name = strcat(pre_name,num2str(i),'.*.dcm');
    S = dir(fullfile(path,file_name));
    file = strcat(path,'\',S.name);

    % Read DICOM file, and calculate the mAs for each file
    info = dicominfo(file);
    z(i) = int16(info.SliceLocation)*(-1);
    mAs = info.XRayTubeCurrent * info.RevolutionTime /
info.SpiralPitchFactor ;
    eff = [eff, int16(mAs)];
end

% Plot
sc = 2;
scatter(z,eff,sc,'filled')
```

Source Code 1: Plot effective mAs vs. Z-position curves for different kVp and pitch settings.

```
Folder = '2';
slices = [14,92,186,247,315];

pre_name = strcat('mercury_phantom.CT.RTP_Thorax_[fac.',Folder, '.');
C = [254, 255];

Dia = [160, 210, 260, 310, 360];
Radius = [68,92,112,133,154];

for n = 1:1:length(slices)

    ROIs = [];
    f_range = 1;
    psize = [0.8, 0.8]; % pixel
    th = linspace(0,2*pi);
    center_x = C(1);
    center_y = C(2);
    edge = 14;
    step = 1;

    File_name = strcat(pre_name,num2str(slices(n)),'.*.dcm');
```

```

S = dir(fullfile(Folder,File_name));
File = S.name;

I = dicomread(strcat(Folder, '\',File));

loop = floor((Radius(n)-edge)/step)-(edge/step)*2;
radius_list = [];
noise_list = [];
for j = 1:1:loop
    radius = 16 + (j-1)* step;
    radius_list = [radius_list, radius*1.18];

    noise = [];

    for k = 1:8
        theta(k) = (k-1)* pi/4;
        centers(:,k) = [int16(center_x+radius * sin(theta(k))),
int16(center_y - radius * cos(theta(k)))];
        ROIs(k,:) = [int16(centers(1,k)-edge/2), int16(centers(2,k)-
edge/2) ,int16(centers(1,k) + edge/2), int16(centers(2,k) + edge/2)];
        noise(k) = std2(I(ROIs(k,1):ROIs(k,3),ROIs(k,2):ROIs(k,4)));
        noise(k);
    end

    Noise = mean(noise);
    noise_list = [noise_list, Noise];
    res = [Dia(n),radius, Noise];
end

X = radius_list;
Y = noise_list;
leg = [num2str(Dia(n)) ' mm'];
plot(X,Y, 'LineWidth',1.5);
hold on;
end

ylabel('Noise');
xlabel('Distance to Center [mm]');
title('Radial Noise Distribution');

hold off;
legend({'160 mm', '210 mm', '260 mm', '310 mm', '360
mm'}, 'Location', 'southeast');

```

Source Code 2. The MATLAB source code to plot radial noise distribution

```

% 160 mm
Folders = ["0006", "0007"];
slice = 4; % The file of each slices
Radius = 104;

% 210 mm
% Folders = ["0008", "0009"];
% slice = 12; % The file of each slices
% Radius = 136;

```

```

% 260 mm
% Folders = ["0010","0011"];
% slice = 13;          % The file of each slices
% Radius = 168;

% 310 mm
% Folders = ["0012","0013"]; % '0007';
% slice = 13;          % The file of each slices
% Radius = 200;

% 360 mm
%Folders = ["0014","0015"]; % '0007';
%slice = 13;          % The file of each slices
%Radius = 230;

C= [254, 255];          % Coordinate of the center
% Dia = [160]; % [160, 210, 260, 310, 360];    % Dimension List

for n = 1:1:length(Folders)

    Folder_Name = strcat('ABDOMEN_3_0_BR38_2_',Folders(n));

    pre_name =
strcat('MERCURY_PHANTOM.CT.ABDOMEN_RT_ABDOMEN_3MM_(ADULT).',Folders(n),'.');

    ROIs = [];          % Region of Interest
    center_x = C(1);    % position of x-center
    center_y = C(2);    % position of y-center
    edge = 10;          % the length of the edge
    step = 1;           % moving step

    % Prepare for the Dicom File Name
    File_name = strcat(pre_name,num2str(slice,'%04d'),'*.IMA');
    S = dir(fullfile(Folder_Name,File_name));
    File = S.name;

    % Read the image from Dicom File
    I = dicomread(strcat(Folder_Name,'\ ',File));

    % Read the header of Dicom File, and calculate mAs,
    % image_slice_thickness
    info = dicominfo(strcat(Folder_Name,'\ ',File));
    mAs = info.XRayTubeCurrent * (str2num(info.SeriesTime) -
str2num(info.AcquisitionTime)) / info.SpiralPitchFactor;
    image_slice_thickness = info.SliceThickness;

    % How many steps need to be excuted, can be adjusted
    loop = floor((Radius-edge)/step) - (edge/step)*2;
    radius_list = [];
    noise_list = [];

    for j = 1:1:loop
        radius = 18 + (j-1) * step;          % 14 is the initial position, can be
adjusted
        radius_list = [radius_list, radius*1.18];
    end
end

```

```

noise = [];

for k = 1:8 % Eight sample zones around the center
    theta(k) = (k-1)* pi/4;
    centers(:,k) = [int16(center_x+radius * sin(theta(k))),
int16(center_y - radius * cos(theta(k)))];
    ROIs(k,:) = [int16(centers(1,k)-edge/2), int16(centers(2,k)-
edge/2) ,int16(centers(1,k) + edge/2), int16(centers(2,k) + edge/2)];
    noise(k) = std2(I(ROIs(k,1):ROIs(k,3),ROIs(k,2):ROIs(k,4)));
end

% Calculate the mean of sample zones
Noise = mean(noise);

% Calculate the Normalized Noise
Normalized_Noise = Noise/(sqrt(200/mAs) *
sqrt(5/image_slice_thickness));

noise_list = [noise_list, Normalized_Noise];

% if you would like to display the result, remove following comments
% res = [Dia(n),radius, Normalized_Noise];
% disp(res);

end

X = radius_list;
Y = noise_list;
max(Y) - min(Y)
plot(X,Y, 'LineWidth',1.5);
hold on;
end

ylabel('Normalized Noise');
xlabel('Distance to Center [mm]');
title('Normalized Noise Distribution (360 mm)');

hold off;
legend({'120 kV', '140 kV'}, 'Location', 'northeast'); %({'160 mm', '210
mm', '260 mm', '310 mm', '360 mm'}, 'Location', 'southeast');

```

Source Code 3. The MATLAB source code to generate normalized noise vs. radius plots.

```

clc;
clear;
% scan_id = '0006'; diameter = '160 mm'; kv = '120';
% scan_id = '0007'; diameter = '160 mm'; kv = '70';

% scan_id = '0008'; diameter = '210 mm'; kv = '120';
% scan_id = '0009'; diameter = '210 mm'; kv = '70';

% scan_id = '0010'; diameter = '260 mm'; kv = '120';
% scan_id = '0011'; diameter = '260 mm'; kv = '100';

```

```

% scan_id = '0012'; diameter = '310 mm'; kv = '120';
% scan_id = '0013'; diameter = '310 mm'; kv = '100';

% scan_id = '0014'; diameter = '360 mm'; kv = '120';
scan_id = '0015'; diameter = '360 mm'; kv = '140';

pre_path = 'ABDOMEN_3_0_BR38_2_';
Folder = strcat(pre_path,scan_id);

pre_name =
strcat('MERCURY_PHANTOM.CT.ABDOMEN_RT_ABDOMEN_3MM_(ADULT).',scan_id, '.');

total_slices =size(dir(Folder),1)-2;

step = 2;

slices = [1:step:total_slices];

C= [255, 254];
ROIs = [];
f_range = 1.2; % the value equals fRange = [0 8] in
npsplot.m line 77
psize = [0.8, 0.8]; % [1.2, 1.2]; % pixel will determine the range of
frequency as well
th = linspace(0,2*pi);
center_x = C(1);
center_y = C(2);
edge = 8;

% Eight zones in a circle

% ny = 1./(2*psize); % Nyquist frequency

n = length(slices);

for i=1:n
file_name = strcat(pre_name,num2str(slices(i),'%04d'),'*.IMA');
S = dir(fullfile(Folder,file_name));
File = S.name;

I = dicomread(strcat(Folder,'\',File));

for j = 1:7

radius = 10 + j*2;
f = [];
nps = [];
noise = [];
fpeak = [];
fav = [];

for k = 1:8
theta(k) = (k-1)* pi/4;
centers(:,k) = [int16(center_x+radius * sin(theta(k))),
int16(center_y - radius * cos(theta(k)))];
ROIs(k,:) = [int16(centers(1,k)-edge/2), int16(centers(2,k)-
edge/2) ,int16(centers(1,k) + edge/2), int16(centers(2,k) + edge/2)];

```

```

        % rectangle('Position',[ROIs(i,1) ROIs(i,2) edge edge])
        [f(:,k),nps(:,k), noise(k), fpeak(k), fav(k)] = npsplot(I,
ROIs(k,:),psize, f_range);
    end

    X(:,i) = mean(f,2);
    Y(:,i) = mean(nps,2);
    Noise = mean(noise);
    Fpeak = mean(fpeak);
    FAV = mean(fav);
    leg{i} = [num2str(slices(i)) ' mm'];
    % res = [Dia(i),radius-5, radius+4, Noise, Fpeak, FAV];
    % disp(res);

end
end

plot(X,Y,'LineWidth',1.5);
legend(leg);
ylabel('NPS [mm^2HU^2]');
xlabel('Spatial Frequency [mm^-1]');
title("Noise Power Spectra (" + diameter + " - "+kv+" kV)");
xlim([0 f_range]);

```

Source Code 4. The MATLAB source code that generate NPS plots.

```

y = [0 0.914 0.987 1.12 1.47]; % Relative Electron Density
% x = [-1005 -87 3.536 528 1447]; % Hounsfield Unit (160mm)
x = [-984 -80 -2.417 472 1300]; % Hounsfield Unit (360mm)
plot(x,y);
hold on

%x = [-1007 -70 1.453 447 1262]; % Hounsfield Unit (160mm)
x = [-985 -62 -4.401 391 1129]; % Hounsfield Unit (360mm)
plot(x,y);
hold on

%x = [-1005 -48 -0.428 341 1059]; % Hounsfield Unit (160mm)
x = [-988 -42 -3.918 287 941]; % Hounsfield Unit (360mm)
plot(x,y);
hold on

%x = [-1004 -37 -0.652 278 938]; % Hounsfield Unit (160mm)
x = [-990 -33 -6.2 226 830]; % Hounsfield Unit (360mm)
plot(x,y);
hold on

%x = [-1005 -29 -1.08 238 867]; % Hounsfield Unit (160mm)
x = [-995 -24 -5.325 190 768]; % Hounsfield Unit (360mm)
plot(x,y);
hold off
xlim([-1100 1100]);
%title('Electron Density Curve shifting (160 mm)')
title('Electron Density Curve shifting (360 mm)')

```

```
ylabel('electron density relative to water')
xlabel('Hunsfield Unit')
legend({'70 kV', '80 kV', '100 kV', '120 kV', '140
kV'}, 'Location', 'southeast');
```

Source Code 5. The MATLAB source code that generated electron density relative to water curve.

Reference

1. McDermott P, Orton C. *The physics & technology of radiation therapy*. 2nd ed. Medical Physics Publishing; 2018.
2. Bushberg JT, Seibert AJ, Leidholdt EM, Boone JM. *The essential physics of medical imaging*. 3rd ed. Lippincott Williams & Wilkins; 2012. <http://cds.cern.ch/record/1425946>.
3. Papadakis AE, Damilakis J. Automatic tube current modulation and tube voltage selection in pediatric computed tomography. *Investigative Radiology*. 2018;54(5):265-272.
https://explore.openaire.eu/search/publication?articleId=od_267::baaedf55c853ae11ca5410dcf5945f7f, doi: 10.1097/rli.0000000000000537.
4. Brinkley MF, Ramirez-Giraldo JC, Samei E, et al. Effects of automatic tube potential selection on radiation dose index, image quality, and lesion detectability in pediatric abdominopelvic CT and CTA: A phantom study. *Eur Radiol*. 2015;26(1):157-166. <https://link.springer.com/article/10.1007/s00330-015-3817-x>. doi: 10.1007/s00330-015-3817-x.
5. Yu L, Bruesewitz MR, Thomas KB, Fletcher JG, Kofler JM, McCollough CH. Optimal tube potential for radiation dose reduction in pediatric CT: Principles, clinical implementations, and pitfalls. *Radiographics*. 2011;31(3):835-848. <https://www.ncbi.nlm.nih.gov/pubmed/21571660>. doi: 10.1148/rg.313105079.
6. Yu L, Li H, Fletcher JG, McCollough CH. Automatic selection of tube potential for radiation dose reduction in CT: A general strategy. *Medical physics (Lancaster)*. 2009;37(1):234-243. doi: 10.1118/1.3264614.

7. Fursevich DM, LiMarzi GM, O'Dell MC, Hernandez MA, Sensakovic WF. Bariatric CT imaging: Challenges and solutions. *Radiographics*. 2016;36(4):1076-1086.
<https://www.ncbi.nlm.nih.gov/pubmed/27232505>. doi: 10.1148/rg.2016150198.
8. Powsner RA, Palmer MR, Powsner ER. *Essentials of nuclear medicine physics and instrumentation*. 3. ed., 1. publ. ed. Chichester: Wiley-Blackwell; 2013. http://deposit.d-nb.de/cgi-bin/dokserv?id=4291896&prov=M&dok_var=1&dok_ext=htm.
9. Filev PD, MD, Mittal PK, MD, Tang X, PhD, et al. Increased computed tomography dose due to miscentering with use of automated tube voltage selection: Phantom and patient study. *Current problems in diagnostic radiology*. 2016;45(4):265-270. <https://www.clinicalkey.es/playcontent/1-s2.0-S0363018815300347>. doi: 10.1067/j.cpradiol.2015.11.003.
10. Timothy P. Szczykutowicz, Phil Michaelson. Using the gammex mercury 4.0™ phantom for common clinical tasks in ct. .
11. Siegel MJ, Schmidt B, Bradley D, Suess C, Hildebolt C. Radiation dose and image quality in pediatric CT: Effect of technical factors and phantom size and shape. *Radiology*. 2004;233(2):515-522.
<https://www.ncbi.nlm.nih.gov/pubmed/15358847>. doi: 10.1148/radiol.2332032107.
12. Funama Y, Awai K, Nakayama Y, et al. Radiation dose reduction without degradation of low-contrast detectability at abdominal multisection CT with a Low–Tube voltage technique: Phantom study. *Radiology*. 2005;237(3):905-910. <https://www.ncbi.nlm.nih.gov/pubmed/16237139>. doi: 10.1148/radiol.2373041643.
13. Nakayama Y, Awai K, Yamashita Y, et al. Abdominal CT with low tube voltage: Preliminary observations about radiation dose, contrast enhancement, image quality, and noise. *Radiology*. 2005;237(3):945-951. <https://www.ncbi.nlm.nih.gov/pubmed/16237140>. doi: 10.1148/radiol.2373041655.

14. Schindera ST, Nelson RC, Mukundan S, et al. Hypervascular liver tumors: Low tube voltage, high tube current multi-detector row CT for enhanced detection—phantom study. *Radiology*. 2008;246(1):125-132. <https://www.ncbi.nlm.nih.gov/pubmed/18096533>. doi: 10.1148/radiol.2461070307.
15. B. Schmidt, R. Raupach, T. Flohr. How to scan with CARE kV. . . <http://siemens.com/healthcare>.
16. Schneider, C. A., Rasband, W. S., & Eliceiri, K. W. NIH image to ImageJ: 25 years of image analysis. . 2012. <https://guides.libraries.uc.edu/imagej>. doi: 10.1038/nmeth.2089.
17. Christianson O, Chen JJS, Yang Z, et al. An improved index of image quality for task-based performance of CT iterative reconstruction across three commercial implementations. *Radiology*. 2015;275(3):725-734. <https://www.ncbi.nlm.nih.gov/pubmed/25686365>. doi: 10.1148/radiol.15132091.
18. MacDougall RD, Kleinman PL, Callahan MJ. Size-based protocol optimization using automatic tube current modulation and automatic kV selection in computed tomography. *Journal of Applied Clinical Medical Physics*. 2016;17(1):328-341. <https://onlinelibrary.wiley.com/doi/abs/10.1120/jacmp.v17i1.5756>. doi: 10.1120/jacmp.v17i1.5756.
19. Davis AT, Palmer AL, Nisbet A. Can CT scan protocols used for radiotherapy treatment planning be adjusted to optimize image quality and patient dose? A systematic review. *British journal of radiology*. 2017;90(1076):20160406. <https://www.ncbi.nlm.nih.gov/pubmed/28452568>. doi: 10.1259/bjr.20160406.
20. Samei E, Bakalyar D, Boedeker KL, et al. Performance evaluation of computed tomography systems: Summary of AAPM task group 233. *Medical physics (Lancaster)*. 2019;46(11):e735-e756. <https://onlinelibrary.wiley.com/doi/abs/10.1002/mp.13763>. doi: 10.1002/mp.13763.
21. Hough DM, Fletcher JG, Mccollough CH, et al. Lowering kilovoltage to reduce radiation dose in contrast-enhanced abdominal CT: Initial assessment of a prototype automated kilovoltage selection tool.

American journal of roentgenology (1976). 2012;199(5):1070-1077.

<https://www.ncbi.nlm.nih.gov/pubmed/23096181>. doi: 10.2214/AJR.12.8637.

22. Finkelstein, Eric A., PhD, MHA, Khavjou OA, MA, Thompson H, BA, et al. Obesity and severe obesity forecasts through 2030. *American journal of preventive medicine*. 2012;42(6):563-570.

<https://www.clinicalkey.es/playcontent/1-s2.0-S0749379712001468>. doi: 10.1016/j.amepre.2011.10.026.

23. Ritter A, Mistry N. Directdensity™ technical principles and implications for radiotherapy. . 2016.

24. McCollough C, Bakalyar DM, Bostani M, et al. Use of water equivalent diameter for calculating patient size and size-specific dose estimates (SSDE) in CT: The report of AAPM task group 220. *AAPM report*. 2014;2014:6-23. <https://www.ncbi.nlm.nih.gov/pubmed/27546949>.